

1

2 Please note that the manuscript has not undergone peer-review and is not accepted for
3 publication at this time. Subsequent versions of this manuscript may have slightly different
4 content. If accepted, the final version of this manuscript will be available via the 'Peer-reviewed
5 Publication DOI link on the right-hand side of this webpage. Please feel free to contact any of the
6 authors; we welcome your feedback on our contribution to the literature.

7

8

On the assessment of sinking particle fluxes from in situ particle size distributions

Elena Ceballos Romero^{1,2}, Ken Buesseler¹, Erik Fields³, Rainer Kiko^{4,5,6}, Meg Estapa⁷, Lee Karp-Boss⁸, Samantha Clevenger⁹, Laetitia Drago⁴, David A. Siegel^{3,10}

¹Woods Hole Oceanographic Institution, Department of Marine Chemistry & Geochemistry, Woods Hole, Massachusetts (USA),

²Department of Applied Physics II, University of Sevilla, Av. Reina Mercedes 4A, 41012, Sevilla, Spain

³Earth Research Institute, University of California, Santa Barbara, Santa Barbara, California (USA),

⁴Sorbonne Université, Laboratoire d'Océanographie de Villefranche, Villefranche-sur-Mer (France)

⁵GEOMAR Helmholtz Centre for Ocean Research Kiel, Kiel, Germany

⁶Faculty of Mathematics and Natural Sciences, University of Kiel, 24148 Kiel, Germany

⁷School of Marine Sciences, University of Maine, Darling Marine Center, Walpole, Maine (USA)

⁸School of Marine Sciences, University of Maine, Orono, Maine (USA)

⁹MIT-WHOI Joint Program in Oceanography, Applied Ocean Science and Engineering, Cambridge, MA, (USA)

¹⁰Department of Geography, University of California, Santa Barbara, Santa Barbara, California (USA)

Corresponding author: Elena Ceballos Romero (eceballos@whoi.edu)

Key Points:

- We assess the performance of UVP-based POC flux estimates using co-located sediment trap and ^{234}Th measurements from EXPORTS campaign.

32 ● UVP flux method explains export variability between sites but not within; key issue is
33 needing a wide POC flux range for its calibration.

34 ● Additional data (e.g., particle morphology and transparency) are needed to improve
35 sinking POC fluxes assessments using in situ imagery.

36 **Abstract**

37 The biological carbon pump is a vital component of the global carbon cycle, particularly through
38 sinking of particulate organic carbon (POC) to the ocean interior. Particle size distribution (PSD)
39 observations from the Underwater Vision Profiler (UVP) have been widely used to quantify
40 sinking POC fluxes. This approach assumes that the sinking POC flux is a function of the PSD
41 multiplied by a power law relating particle size to sinking rates and carbon content. The
42 coefficients of the power law are quantified by regressing UVP data against sediment trap flux
43 observations. Here, we systematically assess the performance of this approach using a large UVP
44 dataset of co-located and coincident sediment trap and thorium-234 flux observations from the
45 North Pacific (50°N, 145°W, August 2018) and the North Atlantic (49°N, 16.5°W, May 2021)
46 sampled during the EXPORTS (EXport Processes in the Ocean from RemoTe Sensing) field
47 campaign, which span both diverse environmental conditions and sinking flux values. Globally,
48 when power law coefficients are evaluated over all sites and depths, the UVP flux method
49 explains 80% of the variance in POC flux. However, when coefficients are determined using
50 regional subsets of the EXPORTS dataset, the method performs poorly. Reasons include lack of
51 knowledge of particle characteristics beyond PSD; undersampling of rare large particles; spatial
52 and temporal scales mismatches between UVPs and flux observations; and difficulties arising
53 from non-steady state conditions. To improve UVP-based sinking POC flux estimates regionally,
54 additional data on particle characteristics such as transparency and morphology are needed.

55 **Plain Language Summary**

56 Anthropogenic CO₂ emissions drive climate change, with the oceanic biological carbon pump
57 (BCP) playing a crucial role in mitigating its impact by transferring photosynthetically fixed carbon
58 from the ocean surface to the deep sea via sinking particles. Understanding the BCP is essential
59 for predicting ocean CO₂ absorption and global carbon cycle impacts. Recent advances in
60 underwater imaging systems, like Underwater Vision Profiles (UVP), allow for tracking particle
61 abundance and offer a means to estimate sinking carbon fluxes alongside traditional methods
62 such as sediment traps and Thorium-234 measurements. Using data collected in the Pacific and
63 North Atlantic oceans, this study compares UVP performance with conventional techniques,
64 finding that while UVP provides global insights, it faces limitations at finer scales, likely due to a
65 lack of information of particle characteristics besides their size, missing rare large particles,
66 mismatched temporal and spatial coverage between techniques, and difficulties in
67 understanding how the changing conditions impact particle fluxes. Ultimately, observations of
68 the particle size distribution from underwater cameras alone do not fully capture the
69 complexities of sinking carbon export fluxes in the ocean.

70 **1 Introduction**

71 The oceanic biological carbon pump (BCP) (Eppley & Peterson, 1979) drives carbon storage in the
72 ocean's interior through the downward flux of biogenic carbon, produced by the net primary
73 production of phytoplankton. There are multiple paths for the BCP (Boyd et al., 2019) but when
74 considering transport to the deep ocean (>1000m) this process occurs primarily through the
75 gravitational sinking of Particulate Organic Carbon (POC) - phytoplankton, zooplankton, detritus,
76 and fecal pellets - from the euphotic zone to deep waters (Boyd et al., 2019; Turner, 2015). While
77 the BCP is a well-recognized driver of atmospheric CO₂ regulation over geological timescales (De
78 La Rocha & Passow, 2007), the precise magnitude of its current contribution to the global carbon
79 cycle, particularly in response to human-induced changes, remains uncertain. Annual carbon
80 export estimates by the BCP vary from 5 to >12 Gt C yr⁻¹ (Boyd & Trull, 2007; Siegel et al., 2023a).

81 Traditional oceanographic techniques, such as sediment traps (e.g., Buesseler et al., 2007) or
82 radioactive disequilibrium methods such as thorium-234 (²³⁴Th half-life, $t_{1/2} = 24.1$ d; e.g.,
83 Buesseler et al., 1992), are resource-intensive and provide limited spatial, vertical, and temporal
84 coverage (Buesseler et al., 2007). The emergence of imaging techniques in recent decades has
85 transformed oceanography (Lombard & Kiørboe, 2010), offering a range of tools to study
86 properties and dynamics of particles across a range of sizes, from micrometers to centimeters,
87 and time scales of seconds depending upon imaging protocols. These technologies, deployable
88 on CTD rosettes from research vessels, autonomous floats, gliders, or moorings, enable
89 observations on oceanographically relevant temporal and spatial scales, while at the same time
90 reducing deployment costs (Giering et al., 2020). Among these, the Underwater Vision Profiler or
91 UVP (Picheral et al., 2010) has become widely used imaging instrument because of its versatility
92 (Kiko et al., 2022).

93 In situ observations of particle size distributions (PSD) from imaging platforms historically served
94 three main purposes: 1) assessing the structural properties of planktonic food webs (Sheldon et
95 al., 1972); 2) inferring particle sinking velocities of individual particle size classes when combined
96 with particle collection traps equipped with polyacrylamide gels (McDonnell & Buesseler, 2010);
97 and 3) estimating sinking particles fluxes (Guidi et al., 2008; Iversen et al., 2010; Kiko et al., 2017).
98 In this study, we revisit and expand this third application of PSD observations using coincident
99 and collocated sinking POC flux determinations with both traps and ²³⁴Th approaches. Each of
100 these methods has strengths and weaknesses including the spatial and temporal scales each
101 represents. Here, we test the assumption that an instantaneous PSD imaged by UVP, essentially
102 a stock measurement, can be related to POC flux, a rate of carbon removal on gravitationally
103 sinking particles.

104 In principle, the sinking POC flux is related to the product of the particle size spectrum and a
105 particle's sinking speed and carbon content, or:

106
$$POC_{flux} = \int_{D_{min}}^{D_{max}} N(D) \rho_{POC}(D) w_s(D) dD \quad \text{Eq. (1),}$$

107 where D is diameter (mm), $N(D)$ is the number concentration of particles as a function of size in
108 differential form (# L⁻¹ mm⁻¹), $\rho_{POC}(D)$ is the POC content of a particle of size D (mg C particle⁻¹),
109 $w_s(D)$ is its sinking rate (m s⁻¹), and D_{min} and D_{max} are the smallest and largest particle sizes
110 resolved, respectively (mm). Unfortunately, we do not know a priori the size dependence of

111 particle sinking rates and POC content. Hence, Eq. (1) is often reformulated by combining the
112 POC content and sinking rate terms into a power function of particle size, resulting in:

113 $POC_{flux} = \int_{D_{min}}^{D_{max}} N(D) A D^B dD$ Eq. (2),

114 where the coefficients, A and B, represent the combined influence of $w_s(D)$ and $\rho_{POC}(D)$, each
115 of which follows a power-law (Alldredge, 1998; Alldredge & Gotschalk, 1988; Lombard & Kiørboe,
116 2010).

117 Guidi et al. (2008) applied equation (2) to calculate POC flux using PSDs in the 250 μm – 1.5 mm
118 size range retrieved from UVPs by optimizing the A and B coefficients using available sinking
119 particle flux observations from sediment traps from sites in the North Atlantic Ocean,
120 Mediterranean Sea and South Pacific Ocean (see Table 2 in Guidi et al. (2008)). This method we
121 will refer to as the “global UVP method” and its application assumes that the power law
122 coefficients are valid globally. Since its introduction, the A and B coefficients from Guidi et al.
123 (2008) have been widely applied to predict POC flux from UVP results in many studies in oceanic
124 settings distinct from the original calibration site of the coefficients (e.g., Forest et al., 2013; Guidi
125 et al., 2009, 2015, 2016; Ramondenc et al., 2016). Recently, Clements et al., (2022) estimated A
126 and B using a machine learning reconstruction of global ocean PSDs determinations tuned against
127 a global compilation of in situ sediment trap and thorium-derived particle flux observations from
128 Bisson et al., (2018) to estimate the sinking POC fluxes from the base of the euphotic zone
129 globally. Although previous authors have highlighted assumptions, caveats, and limitations of this
130 approach, only a few studies (Cram et al., 2022; Fender et al., 2019; Iversen et al., 2010) have
131 modified the global method to estimate region-specific A and B coefficients for different size
132 ranges (see Table 1). The use of regional observations to adjust the model coefficients will be
133 referred to here as the “regional UVP method”. However, a systematic and validated approach
134 for optimizing A and B coefficients to translate UVP-derived PSDs into accurate POC flux
135 estimates across multiple sites and particle flux regimes remains lacking.

136 In this study, we use a comprehensive and unique dataset of PSD observations from UVPs, along
137 with POC flux estimates from sediment traps and ^{234}Th that were co-located in space and time,
138 to evaluate the performance and validity of the global and regional UVP methods. The data were
139 collected together as part of the NASA-funded EXport Processes in the Ocean from RemoTe
140 Sensing (EXPORTS) project at two biogeochemically contrasting sites in terms of POC flux and
141 biogeochemical conditions (Siegel et al., 2021; Johnson et al. 2024). The present PSD datasets
142 also cover an expanded particle size spectrum from 128 μm - 26 mm, which represents a
143 significant broadening in both the scope and methodology of studies using in situ imagery such
144 as UVP to assess sinking export fluxes in the ocean.

145 **2 Materials and Methods**

146 **2.1 Deployments and Setting**

147 The goal of the EXPORTS field campaign is to develop a predictive understanding of the export,
148 fate, and carbon cycle impacts of global ocean net primary production and to assess their impacts
149 in contemporary and future climates (Siegel et al., 2016). Two field campaigns were carried out
150 in two vastly different ocean ecosystems encompassing a wide range of environmental

151 conditions: 1) the North Pacific (NP) at Ocean Station Papa (OSP, 50°N, 145°W) in August-
152 September 2018, and 2) the North Atlantic (NA) in the vicinity of the Porcupine Abyssal Plains
153 Sustained Observatory (PAP, 49°N, 16.5°W) in May 2021. In both field deployments, operations
154 were conducted in three consecutive sampling cycles or “epochs” (E1, E2, and E3 from hereafter)
155 designed to constrain the pathways for organic carbon transformation and export. The length of
156 each epoch was approximately one week with the goal of completing a sequence of observations
157 that could be repeated three times during a given cruise. Conceptually, the aim is to follow how
158 surface properties might be observed to propagate to depth as part of the BCP, i.e., a particle
159 formed at the surface on day 1, would take approximately one week to reach 500 m if settling at
160 roughly 70 m/d (Siegel et al., 2021).

161 The North Pacific site can be characterized as an iron-limited, high-nutrient, low-chlorophyll
162 (HNLC) region of the world ocean, which leads to limited phytoplankton production and surface
163 chlorophyll (Chl-a) concentrations. An overview of the NP sampling plan, including context
164 information on physical and bio-optical properties, nutrients, and phytoplankton biomass, is
165 presented in Siegel et al. (2021). Two ships were deployed during the NP expedition: a Process
166 Ship (*R/V Roger Revelle*, cruise *RR1813*) focused on sampling biogeochemical stocks and fluxes
167 while following a Lagrangian float, and a Survey Ship (*R/V Sally Ride*, cruise *SR1812*) that
168 characterized the spatial distribution of properties surrounding the Process Ship and cross-
169 calibrated sensors onboard the ships and the autonomous platforms (Siegel et al., 2021). Briefly,
170 during our study period the oceanographic setting was typical of late-summer conditions at OSP
171 with low biomass, a highly recycled food web, and low sinking POC export fluxes driven largely
172 by zooplankton processes (McNair et al., 2023; Stamieszkin et al., 2021; Steinberg et al., 2023).
173 Weak horizontal currents and spatial gradients in biogeochemical fields and low level of temporal
174 variability characterized the three sampling epochs (E): E1 (August 14-23), E2 (August 24-31), and
175 E3 (September 1-9). In terms of POC export, the site was characterized by a modest sinking
176 carbon fluxes with an export efficiency at the base of the euphotic zone (ratio of POC flux to net
177 primary production) of ~13% and a flux attenuation in the subsequent 100 m of ~39% (Buesseler
178 et al., 2020a).

179 The North Atlantic site is a highly advective environment dominated by eddies which can cause
180 upper ocean biogeochemical properties to evolve on time and space scales comparable to those
181 driven by biological processes (Johnson et al., 2024). The NA operations were conducted in a
182 coherent, anticyclonic, physically retentive eddy that minimized horizontal exchanges, so that
183 changes in biological or chemical properties were dominated by local rather than advective
184 processes (Johnson et al. 2024). During the NA deployment, a third ship was added to the Survey
185 Ship (*RSS Discovery*, cruise *DY131*) and the Process Ship (*R/V James Cook*, cruise *JC214*), the *R/V*
186 *Sarmiento de Gamboa* (cruise *SdG2105*), that focused on plankton and metazoan imaging. Similar
187 to the NP sensor calibration exercise, a detailed intercalibration was performed on all the NA
188 sensor observations (Siegel et al., 2023b) . In short, the expedition sampled a transition to high
189 sinking particle fluxes as conditions differed for the three sampled epochs. The first epoch (E1;
190 May 5-7) was marked by a very large diatom biomass in the surface ocean but an absence of
191 aggregates in the upper mesopelagic portion of the water column (Romanelli et al., 2024; Siegel
192 et al., 2025). The second epoch (E2; May 11-20) followed a major storm with wind speeds
193 exceeding 40 knots and was marked by a large change in surface properties and the appearance

194 of aggregates. Export flux metrics remained low by most measures until the third epoch (E3; May
195 21-29), which was marked by large increases in both sinking particle fluxes and aggregate
196 abundances (see Brzezinski et al., 2024; Clevenger et al., 2024; Romanelli et al., 2024; Siegel et
197 al., 2025).

198 2.2 Measurements and Biogeochemical Context During EXPORTS

199 *Sediment trap fluxes:* Two types of sediment traps with identical collection tubes (collection area
200 = 0.0226 m²) were used - neutrally buoyant sediment traps (NBSTs) and a surface-tethered
201 sediment trap array (STT). Sinking particles were collected over approximately 2 to 5-day
202 deployments in the upper 500 m of the ocean during the three epochs in each EXPORTS field
203 campaign (Estapa et al., 2021; Johnson et al., 2024). Results from these traps are discussed here
204 without distinction of trap type. Formalin-poisoned brine traps were gravity filtered through 335-
205 micron screens, swimmers were manually removed from the screens under magnification, and
206 the remaining material was recombined with < 335 µm material for bulk elemental analysis for
207 POC. During the NP, sample composition was used to perform an additional correction for POC
208 from small swimmers that could not be removed following screening (Estapa et al., 2021). POC
209 fluxes were modest during E1 and E2, and increased moderately during E3. During NA, particle
210 export flux seen in the traps increased rapidly two weeks after the experiment started, from
211 similarly low fluxes in E1 and E2 to high fluxes in E3, suggesting strong temporal variability in flux
212 (Clevenger et al., 2024; Romanelli et al., 2024).

213 *234-Thorium POC fluxes:* The ²³⁴Th disequilibrium relative to uranium-238 (²³⁸U) in depths ranging
214 from 0 to 500 m was used during EXPORTS to estimate POC fluxes following the methodological
215 approach proposed by Buesseler et al. (1992). A description of the analytical method can be
216 found in Clevenger et al. (2021). A full description of ²³⁴Th measurements and derived fluxes from
217 the NP and NA experiments can be found in Buesseler et al. (2020a) and Clevenger et al., (2024),
218 respectively.

219 During the NP, the spatiotemporal variability of ²³⁴Th activity was fairly consistent within each
220 epoch, which supported the use of a steady state interpretation of the deficits (Buesseler et al.,
221 2020a), an approach that reduces uncertainties related to error propagation over short
222 timescales (Ceballos-Romero et al., 2018; Savoye et al., 2006). The NP ²³⁴Th observations show
223 relatively homogenous and consistent ²³⁴Th disequilibria, with higher ²³⁴Th fluxes observed at
224 depths of 50 to 100 m, remaining relatively constant or decreasing at greater depths in the water
225 column (see Figures 1 and 2 in Buesseler et al., (2020a)). ²³⁴Th-derived POC fluxes showed a
226 similar trend, but with fluxes decreasing more sharply with increasing depth during all epochs.

227 During NA, the magnitude of ²³⁴Th disequilibria varied both temporally and spatially through the
228 cruise. However, ²³⁴Th-derived POC fluxes revealed minimal to no attenuation with depth across
229 all three epochs, with fluxes at 100 m persisting with similar or even slightly higher values at
230 deeper waters (see Figure 3 in Clevenger et al., 2024). Existing ²³⁴Th deficits indicated that particle
231 fluxes had been high prior to the start of the cruise (Clevenger et al., 2024). Since ²³⁴Th
232 measurements are integrated over time rather than an instantaneous representation of a
233 system, a non-steady state model was needed to derive POC fluxes that increased during the
234 experiment.

235 *In Situ Observations of Particle Size Spectra:* The 5th generation of underwater cameras (UVP5;
236 Picheral et al., (2010)) was used to collect all PSD data used here. A total of 387 high-resolution,
237 full depth profiles of particle size spectra were sampled with five different UVPs mounted on the
238 bottom of each ship CTD-Rosette (169 and 218 in the NP and NA, respectively; see Table 1). The
239 UVP5 captures and processes images of particles (living and non-living) in real time at a rate up
240 to 6 Hz using two collimated red light-emitting diodes (LEDs) that illuminate a well-defined
241 volume of ~1 L with each 100 μ s flash. Particles are detected and sized based on their projected
242 area and converted to equivalent spherical diameter (ESD). Here, particle counts and binned into
243 logarithmically distributed size bins ranging from 128 μ m to 26 mm, although it is recognized the
244 largest few bins will very rarely if ever contain any particles. This range of bins was chosen to
245 ensure consistent data quality and comparability across the five UVP5 units used (details on the
246 UVP5 intercalibration procedure are available in Siegel et al., (2023b) and summarized in the
247 Supporting Information, SI; Section S1). Particle counts were obtained from the downcast of each
248 CTD cast, converted to particle size spectra, $N(D)$, by normalizing by bin width and then
249 aggregated into 5-m depth averages. Based upon the CTD's lowering rate (~1 m s⁻¹), the UVP5's
250 sampling rate (20 Hz) and its sampling volume (~1 L), it is estimated that each 5-m PSD
251 determination represents an average of ~100 L.

252 2.3 Determination of Sinking POC Fluxes from UVP PSD Observations

253 We estimate the values and uncertainties for the coefficients A and B in equation (2) using
254 independent POC flux estimates from both trap and ^{234}Th fluxes using a nonlinear least squares
255 regression procedure. Fits were made using all available EXPORTS observations and depths, the
256 "global UVP method" as well as using data from the NA and NP deployments separately, the
257 "regional UVP method". Initial work fitting coefficients for individual epochs were conducted, but
258 the results were poor; likely due to the very limited number of data points available (as few as 5
259 for ^{234}Th and 9 for sediment traps; Table S1). Several considerations arise concerning how data
260 are used to fit coefficients A and B , including the UVP size range selected for fitting, the selection
261 of UVP and flux determinations to be used, and the vertical resolution used.

262 *Particle size range considerations* - Guidi et al. (2008)'s original application of the UVP flux
263 method used data from older UVP models (UVPs 2, 3, and 4) that were processed into an
264 overlapping size range from 0.25 to 1.5 mm across 8 standardized size bins (see Tables 2 and 3 in
265 Guidi et al., (2008) for details). With advances in the UVP5 model (Picheral et al., 2010), a wider
266 size range of sizes are available from 128 μ m to 26 mm across 23 standardized size bins. The
267 wider range of bins is used as larger particle sizes which should make a greater contribution to
268 the total POC flux (Durkin et al., 2021; Laurenceau-Cornec et al., 2020) and hence, the potential
269 for better performance. To compare with the original study by Guidi et al., (2008), we did a global
270 optimization using the original 8 size bins with the EXPORTS data set. For all cases, we did not
271 attempt to correct for potential all living and non-living particles, consistent with most previous
272 studies.

273 *Sediment trap considerations* - For the consideration of the spatial scales for the NP traps, we
274 only matched UVP profiles and trap fluxes from the same source funnel, as described in Estapa
275 et al., (2021). In essence, choosing only UVP profiles falling within the particle source region

276 defined by local currents and assuming a conservative particle sinking rate of 100 m d⁻¹ (e.g.,
277 Siegel et al. 2008). In the NA, the spatial criterion was related to the dimensions of the core of a
278 retentive eddy that was sampled during the experiment in a Lagrangian fashion (Erickson et al.,
279 2023; Johnson et al., 2024). In this case, only UVP profiles and trap flux observations within the
280 eddy center waters were used (defined as ≤ 15 km from the analyzed eddy center; Johnson et al.
281 2024).

282 *Thorium-234 flux considerations* - As both UVP images and ^{234}Th samples were collected on the
283 same CTD cast, paired UVP and ^{234}Th observations were used to construct the global (both NA
284 and NP) and regional (NP or NA separately) estimates of A and B . All available pairs were used in
285 the NP as there was little discernable spatial variability (Buesseler et al., 2020a). However, for the
286 NA, we restricted the ^{234}Th and UVP matchups to the eddy center, consistent with the approach
287 used for the trap data.

288 *Vertical Resolution Considerations* - The three data sets used all have different vertical resolutions
289 in their sampling. For comparisons to a specific trap depth or ^{234}Th measurement, we used the
290 average of the 5-m resolution UVP data at the measurement depth and the three 5-m depth
291 intervals above it. This resulted in a 20-m depth average, corresponding to imaging roughly 400
292 L of seawater. No data above the mixed layer depth (MLD) were considered, as this layer typically
293 marks the upper boundary for net particle export from the surface ocean. This is especially true
294 when the MLD is deeper than the particle production zone, in which case suspended and sinking
295 particles are physically mixed below the euphotic zone (Buesseler et al., 2020b).

296 *Optimization procedure and uncertainty calculations* – Estimates of the A and B coefficients were
297 determined using the *nlnfit.m* routine in Matlab (Natick, MA, USA), which uses the Levenberg-
298 Marquardt algorithm (Seber & Wild, 2003). Uncertainty bounds are calculated as the 95%
299 confidence intervals using the variance-covariance matrix of the fitted coefficients. Confidence
300 intervals for the fit parameters and several goodness of fit metrics, such as the coefficient of
301 determination for the linear fit (r^2), the normalized root mean square error (nRMSE), are
302 reported in Table 1. The mean bias was calculated, but it is omitted from Table 1 because it was
303 zero.

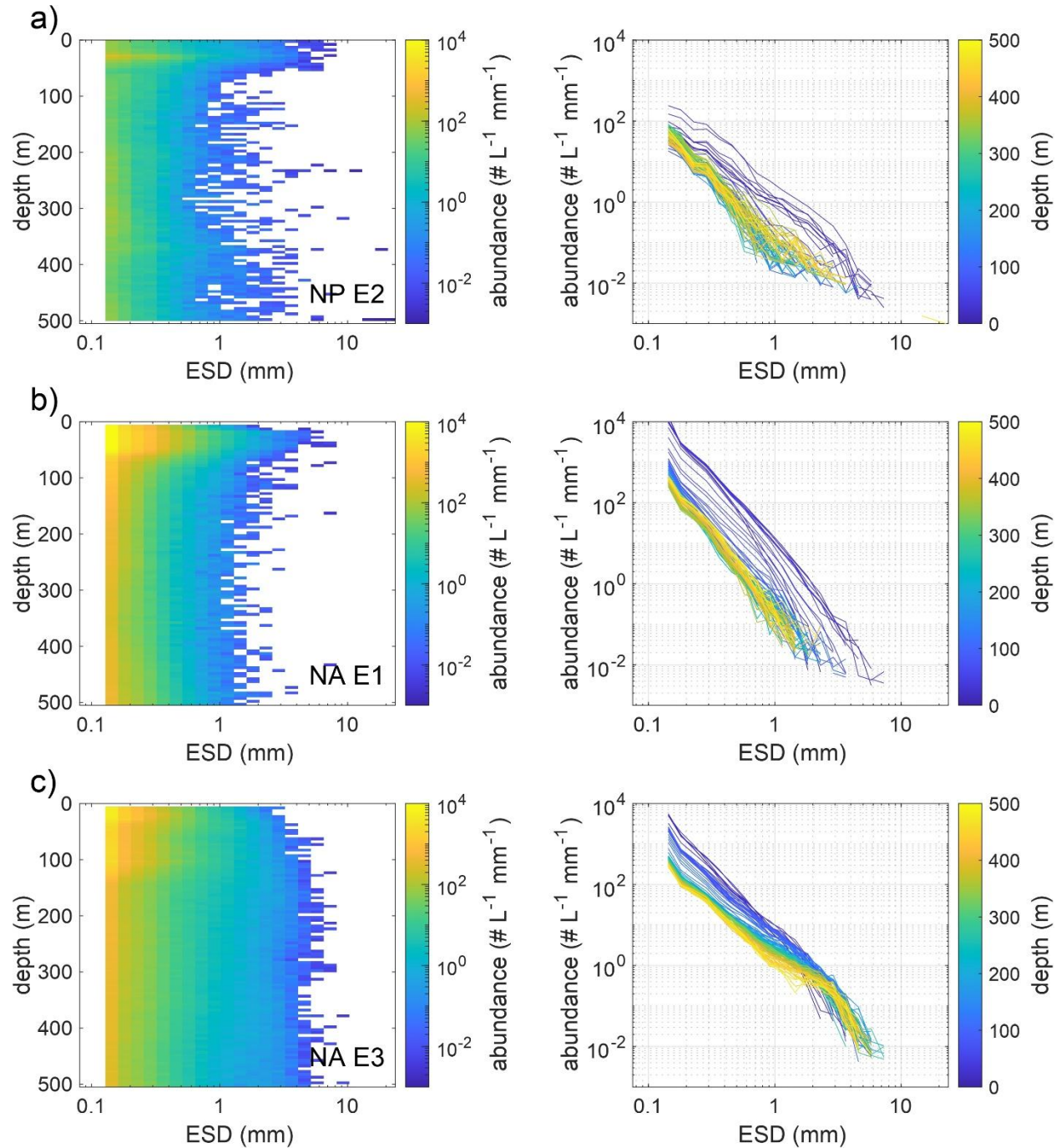
304 We note that, as highlighted in Clements et al., (2023), the coefficients A and B are not entirely
305 independent during fitting, and compensation between the two can lead to similar flux estimates
306 from different parameter combinations. This trade-off introduces uncertainty in the
307 interpretation of A and B and suggests that any comparisons of their values should be made with
308 caution. In this study, our focus remains on how optimized combinations of A and B reproduce
309 observed POC fluxes rather than interpreting the coefficients individually.

310 **3 Results**

311 **3.1 PSD Observations**

312 Example profiles PSD spectrum of in situ particle abundance (# L⁻¹ mm⁻¹) as a function of ESD
313 (mm) and depth are shown in Figure 1. In the NP, UVP-PSD observations exhibit little discernible

314 temporal variations (Figure 1a and S1a). Conversely, in the NA, PSDs changed throughout the
 315 cruise (Figure 1b, 1c, and S1b).



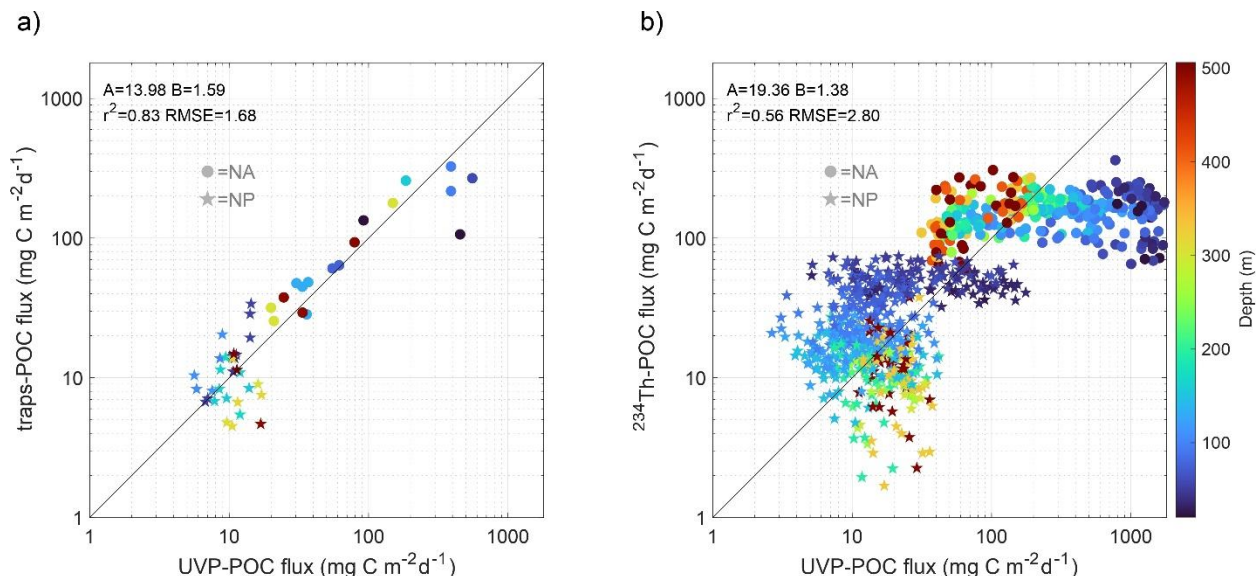
316
 317 **Figure 1.** Example particle size distribution (PSD) profiles for selected epochs plotted against aggregate equivalent
 318 spherical diameter (ESD, mm) and depth for the a) NP and b-c) NA. For each panel, the figure on the left shows ESD
 319 versus depth, the color bar indicates particle abundance for each size (in $\# L^{-1} mm^{-1}$, logarithmic scale). Red
 320 indicates a higher number of particles than blue. The figure on the right shows ESD versus abundance, the color bar
 321 indicates depth (m). Red indicates deeper waters than blue. For the NP, few discernable changes in PSD were observed
 322 over time and a random profile in E2 was chosen. For the NA, PSD evolved between epochs and representative profiles
 323 early (E1) and late (E3) in the cruise are shown.

324 As expected, particle abundance decreases with increasing size for all casts in both experiments,
 325 with smaller particles being more abundant than large ones by several orders of magnitude at all
 326 depths. However, distinct vertical patterns emerge for each experiment based on the particle
 327 size. Note also that there very few particles measured by the UVP with ESD > 5 mm.

328 In the NP, abundances of small particles remain relatively consistent across depths and time,
 329 whereas larger particles decreased in abundance with depth and were constant at lower
 330 abundances below 100 m (see right panel in Figure 1a). In the NA, the PSD changed both over
 331 time and depth (see Figure 1b and 1c). During the initial days of the experiment (E1), small
 332 particles were highly concentrated in the surface layer (0-50 m) and decreased with depth, while
 333 deeper layers showed a shift toward fewer, larger particles. In the later stages of the experiment
 334 (E3), there was a substantial increase in large particles, especially at depth.

335 3.2 A and B Coefficients using EXPORTS Results

336 When applying the global approach using traps, i.e. calibrating all data from both sites for a single
 337 A and B value, no significant differences were observed within the uncertainty bounds in the
 338 retrieved A and B coefficients using either 8 or 23 size bins (Table 1). However, the ratio of
 339 uncertainty to estimate is > 1 for the 8 bins (SI, Figure S2). Hence, we only consider 23 size bin
 340 models in our comparisons below ($A = 13.98 \pm 5.78 \text{ mg C d}^{-1} \text{ mm}^{-8}$, $B = 1.59 \pm 0.44$, $r^2 = 0.83$,
 341 Figure 2a). When applied to ^{234}Th POC flux determinations, the global model has a poorer fit with
 342 a somewhat larger value of A though a similar B ($A = 19.36 \pm 2.85 \text{ mg C d}^{-1} \text{ mm}^{-8}$, $B = 1.38 \pm 0.15$,
 343 $r^2 = 0.56$; Figure 2b). Using sediment traps, the NA regional approach produced A and B
 344 coefficients similar to those from the global approach, with differences falling within uncertainty
 345 bounds. However, in the NP, the regional model showed no predictive power using traps ($r^2 = 0.04$).
 346 When using ^{234}Th , neither the NP or NA exhibited regional predictive capability ($r^2 = 0.08$
 347 and 0.02, respectively; Table 1).



348
 349 **Figure 2.** Results of the global models for UVP-based POC fluxes (in $\text{mg C m}^{-2} \text{ d}^{-1}$, x-axis) using a) traps and b) ^{234}Th
 350 (y-axis) using the global approach for 23 size bins (128 μm – 26 mm). Indicated in each panel along with the r^2 of
 351 the linear fit and the nRMSE. The biases are not shown because they are zero for all fits. Goodness of fit statistics

352 and 95% CIs for the *A* and *B* coefficients are provided in Table 1. Stars represent the NP results, and circles the NA
353 results, with color representing depth (in m). The black line indicates the 1:1 line.

354 3.3 Vertical Profiles of POC flux

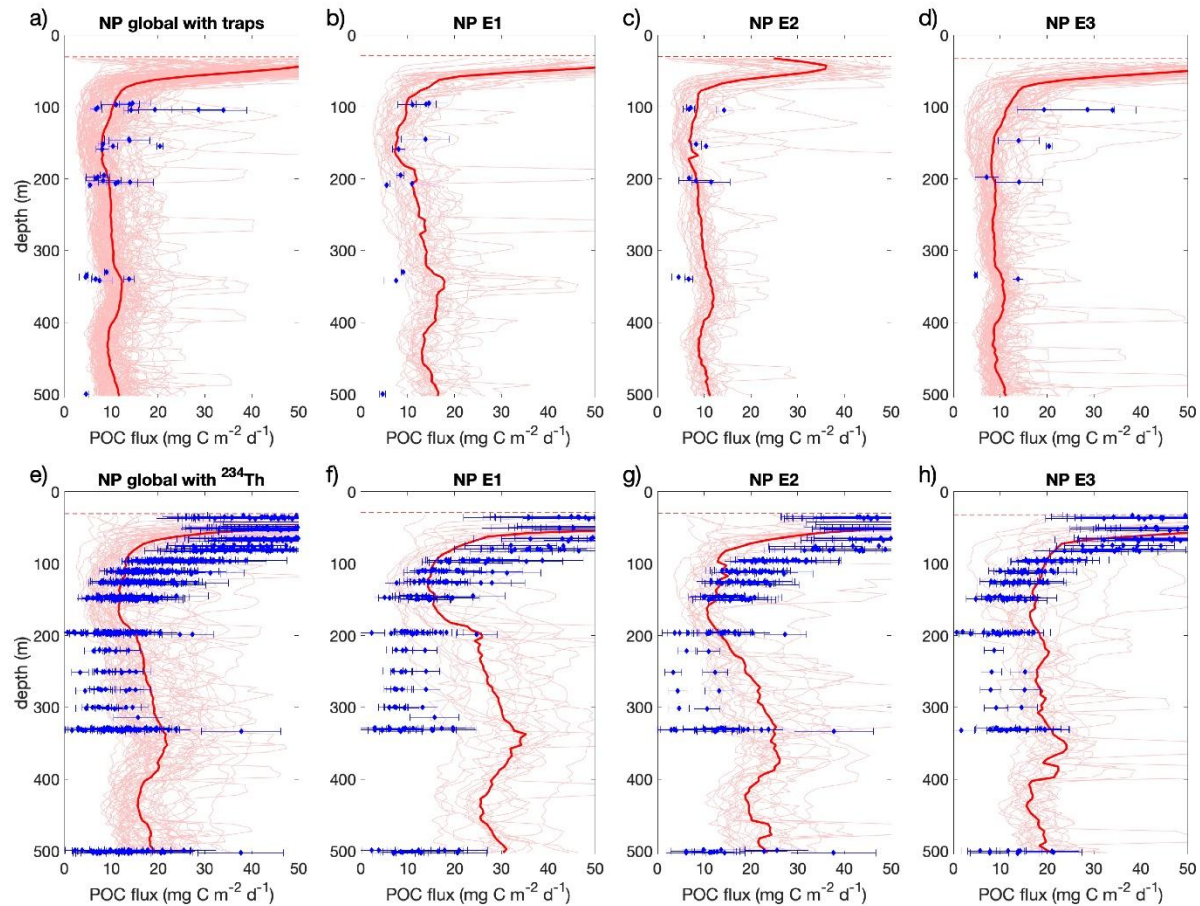
355 Using the *A* and *B* values from EXPORTS, we can derive vertical profiles of POC flux from any given
356 UVP profile in that study (Table 1). Figures 3 and 4 show the variability in UVP derived flux profiles
357 for both the global (panels a and e) and regional (panels b-d and f-h) fit parameters for the NP
358 and NA, respectively. Concurrent trap and ^{234}Th flux profile observations are overlain in the upper
359 and lower rows of Figures 3 and 4, respectively. In each case, the flux profiles using UVP data
360 show both extreme vertical variability and large cast to cast variability (red lines).

361 For the NP, UVP fluxes range from 5 to 50 $\text{mg m}^2 \text{ d}^{-1}$ (global calibration against all traps; Figure
362 3a), with an average around 50 $\text{mg m}^2 \text{ d}^{-1}$ below the MLD decreasing to vertically uniform values
363 of $\sim 10 \text{ mg m}^2 \text{ d}^{-1}$ below 100 m. Note however individual UVP casts even in the upper 50-100 m
364 can have lower or higher fluxes predicted than these averages. The fit of the UVP average with
365 the observational trap results in the NP is good within the spread of the trap data (Figure 3a).
366 Similar patterns are found for the UVP fluxes calibrated with the ^{234}Th observations, although the
367 fluxes are > 1.5 times higher, reflecting the higher values of *A* used (Figure 3d).

368 In principle, a regional calibration of *A* and *B* and concurrent UVP and flux observations might be
369 expected to improve the matchups; however, that is not the case. Using regionally derived
370 models for the NP separated by epoch (Figures 3b-d), the UVP POC flux exceeds the traps around
371 350 m in E1 and E2 (Figures 3b and 3c), and the increase in trap flux in E3 at 100 m is not captured
372 in the E3 UVP profiles (Figure 3d). Small scale changes in flux versus depth or time are thus not
373 improved by using a regional fit to the NP trap data. Considering the NP regional model derived
374 from ^{234}Th , individual ^{234}Th flux profiles vary cast to cast, but not over as wide a range as the UVP
375 derived fluxes (Figures 3f-h). A decrease in flux versus depth is seen in both UVP and ^{234}Th results,
376 but with the UVP showing higher values on average at deeper depths (Figure 3e). A subsurface
377 peak at a depth of ~ 350 m is observed in the ^{234}Th optimized UVP fluxes for all three epochs and
378 is especially strong in the NP E1 (Figure 3f), which may be related to zooplankton diel vertical
379 migration, a process that Amaral et al., (2022) , using inversion analysis of large volume pumped
380 POC samples, showed can significantly contribute to large particle flux in the upper mesopelagic
381 (see their Figure 12). Also, while ^{234}Th fluxes generally increase to some maximum value in the
382 subsurface (here 50 m) and then decrease, UVP derived fluxes always are highest in the
383 shallowest depths.

384 In principle, a regional calibration of *A* and *B* and concurrent UVP and flux observations might be
385 expected to improve the matchups; however, that is not the case. Using regionally derived
386 models for the NP separated by epoch (Figures 3b-d), the UVP POC flux exceeds the traps around
387 350 m in E1 and E2 (Figures 3b and 3c), and the increase in trap flux in E3 at 100 m is not captured
388 in the E3 UVP profiles (Figure 3d). Small scale changes in flux versus depth or time are thus not
389 improved by using a regional fit to the NP trap data. Considering the NP regional model derived
390 from ^{234}Th , individual ^{234}Th flux profiles vary cast to cast, but not over as wide a range as the UVP
391 derived fluxes (Figures 3f-h). A decrease in flux versus depth is seen in both UVP and ^{234}Th results,
392 but with the UVP showing higher values on average at deeper depths (Figure 3e). A subsurface

393 peak at a depth of \sim 350 m is observed in the ^{234}Th optimized UVP fluxes for all three epochs and
 394 is especially strong in the NP E1 (Figure 3f), which may be related to zooplankton diel vertical
 395 migration, a process that Amaral et al., (2022) , using inversion analysis of large volume pumped
 396 POC samples, showed can significantly contribute to large particle flux in the upper mesopelagic
 397 (see their Figure 12). Also, while ^{234}Th fluxes generally increase to some maximum value in the
 398 subsurface (here 50 m) and then decrease, UVP derived fluxes always are highest in the
 399 shallowest depths.

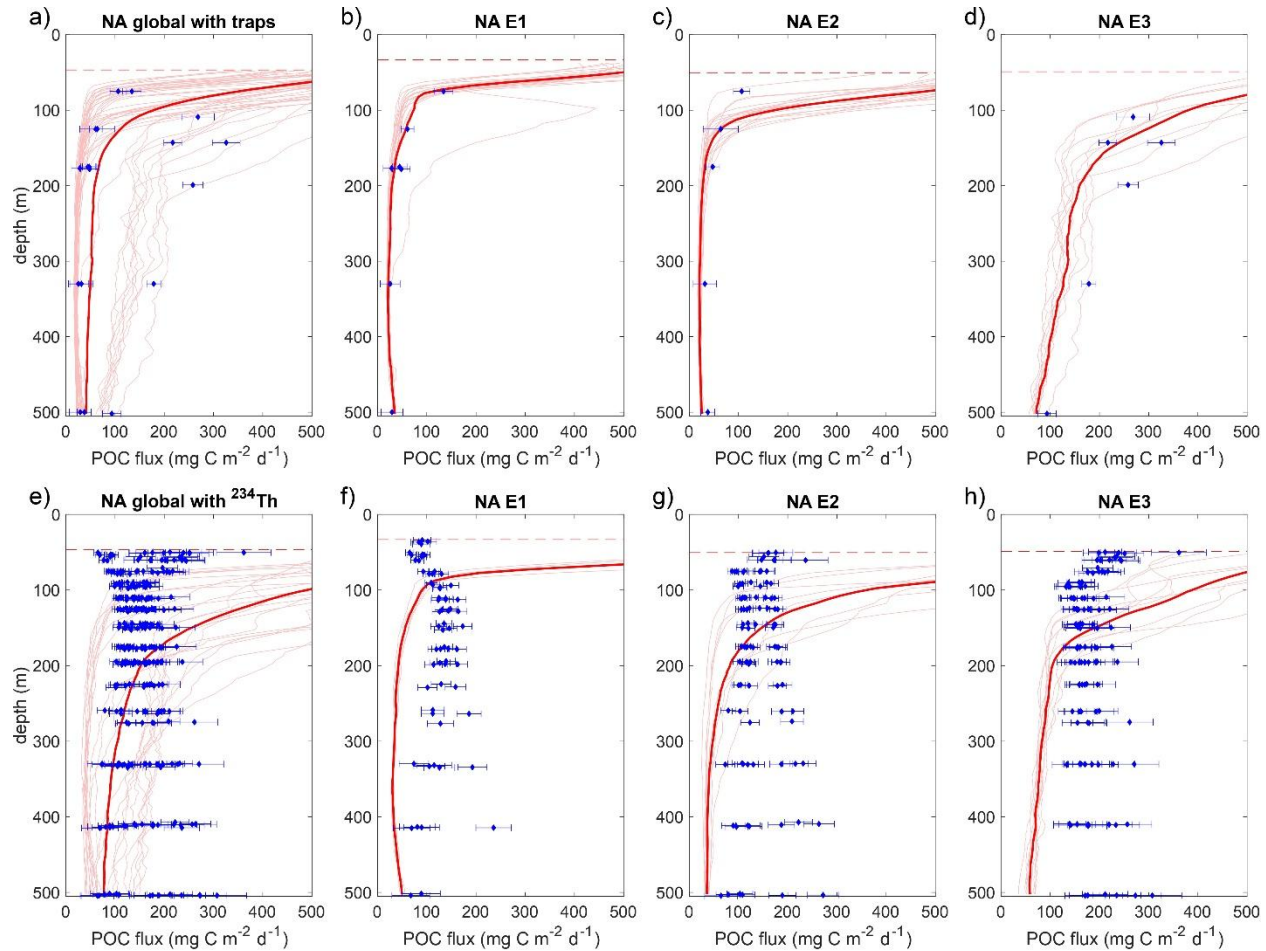


400
 401 **Figure 3.** Vertical profiles of POC fluxes for (a) the global and (b-d) regional approaches in the NP using traps grouped
 402 by epochs: E1, E2, and E3 (from left to right) where the blue diamonds denote sediment trap POC fluxes with
 403 uncertainties from Estapa et al., (2021). Panels (e-h) show the corresponding UVP fluxes optimized using ^{234}Th data
 404 while the gray lines show the ^{234}Th -derived POC flux and the fluxes for each cast, and the black lines show the mean
 405 flux. The horizontal dashed line indicates the mean mixed layer depth over the course of the experiment. Pink lines
 406 show the UVP-based POC flux for each UVP cast, calculated using the A and B coefficients derived from each
 407 approach. Only UVP casts paired with trap or ^{234}Th profiles that fall within an epoch are shown. In panels (a) and (e)
 408 the red line represents the cruise mean UVP-based POC flux of all casts used for the fitting, which includes casts
 409 within a 100 md^{-1} source funnel region (see main text for details). In the rest of the panels, the red line indicates the
 410 epoch mean.

411 In the NA, applying the global trap-based model to UVP data yields flux estimates that are larger
 412 and more variable than in the NP (Figure 4a). As noted previously, the progression of the bloom
 413 resulted in large local changes in particle properties, and this is illustrated clearly when the NA

414 results are displayed for each epoch. Using the NA regional calibration of the UVP data with traps,
 415 there is a better fit between UVP fluxes and traps if broken down by epoch, for which the flux
 416 values increase dramatically in E3, especially at depths > 100 m (Figures 4e versus Figures 4c and
 417 4d).

418 The global model using ^{234}Th data in the NA results in higher UVP fluxes on average (Figure 4e)
 419 and a predicted increase in flux using matched UVP profiles and regional model in E3 (Figure 4,
 420 panels f-h). However, the shape of the two flux profiles differs, with a higher flux at the surface
 421 and steeper flux attenuation evident in the UVP data but not in ^{234}Th results.



422
 423 **Figure 4.** Corresponding figure to Figure 3 for the NA deployment. Casts used for the fitting include only those within
 424 the eddy center.

425 **4 Discussion**

426 We set out to assess the quality of POC flux estimates derived from the UVP imagery using
 427 concurrent sediment traps and ^{234}Th flux observations from the EXPORTS field campaign. The
 428 challenges are substantial given the multitude of issues presented. First, UVP PSD determinations
 429 are at best measures of sinking and non-sinking particles and living stocks, within certain size
 430 ranges and over scales set by the number of images (Hz), imaging volume (liters) and duration of
 431 a CTD cast (hours; meters) (Picheral et al., 2010; 2022). Traps measure the gravitational sinking

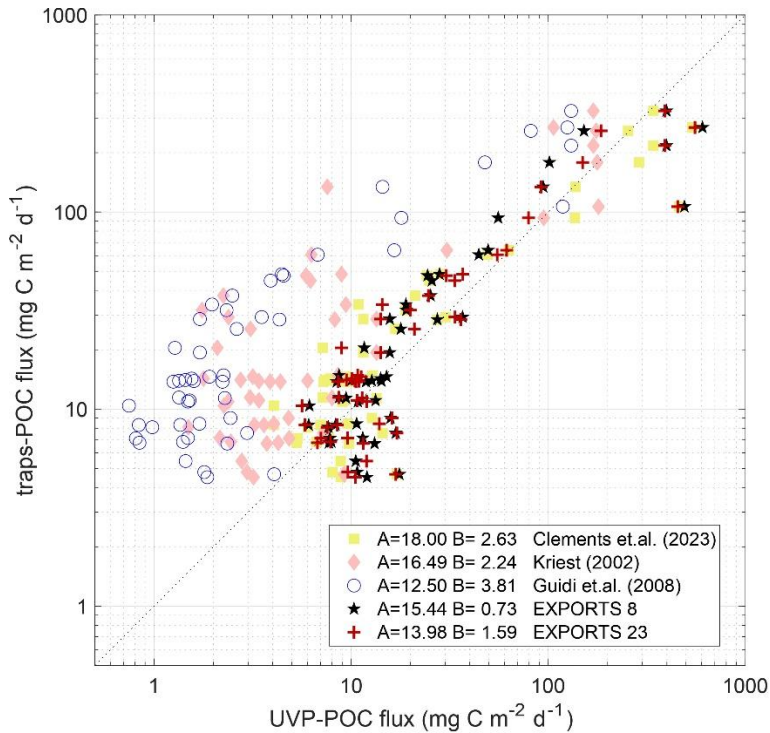
432 flux of particles, largely non-living, and originating from a large particle source area (Siegel et al.,
433 2008) determined by sinking rates, currents and deployment durations (several days; 10's km²).
434 Biases in trap fluxes occur due to hydrodynamics, swimmers, preservation and other issues
435 (Buesseler et al., 2007). The ²³⁴Th flux method tracks small scale variations in flux (km) but
436 averaged over days to weeks. The ²³⁴Th-derived POC flux depends on the measured ²³⁴Th
437 disequilibrium and generally ignores physical processes, but importantly here, the flux can be
438 sensitive to whether a system is at steady state or not, over the course of its half-life (24.1 d)
439 (Ceballos-Romero et al., 2018; Clevenger et al., 2024; Savoye et al., 2006). A conversion from
440 ²³⁴Th flux to POC flux also requires consideration of observed variations in its ratio to POC on
441 particles that vary with depth and location (Buesseler et al., 2006). So, mismatches between UVP,
442 trap and ²³⁴Th estimates of POC flux are expected to be due to a combination of methodological
443 consideration and their respective spatial and temporal averaging.

444 The EXPORTS project provides a unique opportunity to evaluate the utility of UVP-derived flux
445 estimates using an extensive set of co-located and simultaneous sediment traps and ²³⁴Th
446 observations. A key finding is that UVPs can be effectively trained to translate observed PSD
447 changes into POC fluxes when the range in POC fluxes spans several orders of magnitude, and
448 when stocks and fluxes are roughly near steady state. However, when POC flux variations are
449 smaller than an order of magnitude, i.e., at local scales, or are in non-steady state conditions,
450 UVP flux determinations can have large uncertainties. Here, we delve into the findings that led
451 us to these insights.

452 4.1 Comparisons of Global Models

453 The globally optimized A and B coefficients found during EXPORTS using traps were 13.98 and
454 15.44 for A, and from 0.73 are 1.59 for B, respectively for the 8 and 23 size bin models (Table 1).
455 Other global estimates from Clements et al., (2023); Guidi et al., (2008); and Kriest (2002) range
456 from 12.5 to 18.0 for A, and 2.2 to 3.8 for B (Table 1). All of these have considerable uncertainty,
457 particularly for our estimate derived using only 8 size bins.

458 Importantly, our analysis shows that even small differences in the A and B coefficients lead to
459 significant differences in POC fluxes predicted from UVP data (Figure 5), despite the potential
460 compensation between the two parameter values during fitting (Clements et al., 2023). These
461 differences are primarily driven by the B coefficient, which is more sensitive to the particle size
462 range than the A coefficient. Applying the global A and B values derived by Guidi et al., (2008) to
463 our data consistently underestimates trap-measured POC fluxes by an order of magnitude,
464 particularly at lower flux values (Figure 5). Using regionally derived A and B coefficients leads to
465 even larger differences, as shown by applying regional models from the NP and the NA in
466 EXPORTS, as well as from previous studies such as Iversen et al. (2010), Fender et al. (2019), or
467 Forest et al. (2013). However, the comparison is excellent using Clements et al., (2023)'s A and B
468 coefficients applied to the EXPORTS data set.



469

470 **Figure 5.** Results of the matchups between UVP-based POC fluxes (in $\text{mg m}^{-2} \text{d}^{-1}$, x-axis) and sediment trap fluxes (y-axis) using five different sets of A and B coefficients from previous studies and our own, applied to the entire 471 EXPORTS data set. The coefficients used are from: 1) Clements et al. (2023) (yellow squares), 2) Kriest (2002) 472 (orange diamond), 3) Guidi et al. (2008) (blue circles), and the coefficients obtained in our study for the global approach using 473 traps with 4) the same 8 size bins as used by Guidi et al. (2008) (black stars), and 5) 23 size bins (red cruxes; See 474 Table 1).

475 We attribute differences in the *A* and *B* coefficients primarily to differences in particle 476 characteristics found during the EXPORTS deployments, compared to the prior studies (SI, Figure 477 S3). In particular, different depth ranges were considered, which is especially important since a 478 single *A* and *B* values are applied at all depths. Both Guidi et al. (2008) and Iversen et al. (2010) 479 focused on deeper sinking aggregates (100–1000 m, and 1200–1900 m depth respectively) than 480 our study (MLD – 500 m depth). Coefficient *A* represents the product of sinking speed and POC 481 content, while coefficient *B* is linked to the fractal dimension, which describes particle shape 482 complexity. An increase in fractal dimension with depth implies a decrease in particle porosity 483 (Logan & Wilkinson, 1990), which could account for their higher *B* values (3.81 and 4.27, 484 respectively), as the physical compression of aggregates due to fluid dynamics can compact them 485 decrease porosity (Logan & Kilps, 1995). Our EXPORTS results, which show lower *B* values (all 486 values <1.6), suggest the presence of more porous particles, likely aggregates, in the upper 500 487 m for both the NP and NA deployments.

488 We also considered whether changes in *A* and *B* reflect genuine variations in particle 489 characteristics rather than an artifact of the size range used by the imaging systems in different 490 studies. Our 8 bin size range was chosen to match Guidi et al. (2008), and yet Guidi et al. (2008)'s 491 *B* value is 5 times higher (3.81 versus 0.73; Table 1). Therefore, we do not think size range is the 492 primary reason here for differences in *A* or *B* values, rather it is more likely to be attributed to 493 unaccounted for differences in particle characteristics.

495 Another aspect of UVP size ranges is that, at the smaller end, there can be an undercount of the
496 more abundant particles as one reaches the resolution limit (Stemmann & Boss, 2012). Here, the
497 smallest bin considered is 128 μm , which is several times larger than typical pixel size of UVP5
498 imagery (Picheral et al., 2010), so this should not be an issue. Importantly, about 50% of the
499 cumulative particle size distribution occurs near 0.2 mm ESD (see Figures 1 and S1), indicating
500 that the calculated flux is strongly dominated by these smaller particles. At the larger size ranges,
501 > 0.8 mm to 26 mm, the total particle counts drop off and only rarely are particles larger than 10
502 mm observed (Figures 1 and S1). One reason we combine UVP images into 5-m depth bins is to
503 increase imaging volume, and hence our chances quantifying these larger size bins. Additionally,
504 we cannot rule out the contribution of zooplankton to the upper end of the size spectrum.

505 4.2 Comparison of Regional Models

506 Our assumption in creating the regional UVP flux models was that regional differences in particle
507 characteristics would influence the retrieved values for the *A* and *B* coefficients. However,
508 optimizing the *A* and *B* parameters to regional data sets led to higher uncertainty in UVP-based
509 POC fluxes (Table 1). This is likely due to the smaller range of flux values found within each
510 regional subset. Thus, while UVP flux calibration can still be done at regional levels, results should
511 be interpreted carefully. For instance, we attribute the lack of predictive power in the regional
512 calibration in the NP - regardless of whether traps or ^{234}Th are used (Table 1) - to the minimal 754
513 spatial and temporal variations in POC flux during the experiment. In the NA we see a higher
514 range and variation in POC flux, which improved the flux calibrations using UVP and traps (Table
515 1). In sum, we consider UVPs well-suited for understanding large scale POC flux differences across
516 multiple orders of magnitude; however, this approach is less effective at refining small-scale or
517 short-term export rates, especially if strong flux variations do not occur locally or temporally.

518 4.3 Assessing the UVP Modeled POC Fluxes versus Depth

519 4.3.1 Insights from the NP

520 The UVP fluxes, whether derived from global or regional models optimized using trap or ^{234}Th
521 fluxes, performed poorly for the NP (Table 1). During the NP deployment, temporal changes in
522 export were minimal, and the system exhibited largely steady state conditions in water mass
523 properties, production rates, chlorophyll concentrations, particle stocks (McNair et al., 2023;
524 Siegel et al., 2021), and UVP PSD profiles (Figures 1, 3 and S1). Both trap and ^{234}Th results show
525 no noteworthy changes in POC fluxes between E1 and E2, with only small increases detected by
526 traps in E3 (Buesseler et al., 2020a; Estapa et al., 2021). This suggests that conditions in the NP
527 were relatively constant with respect to POC fluxes.

528 Sinking particle characteristics during the NP deployment varied both with depth and across the
529 three deployment periods (Durkin et al., 2021; McNair et al., 2023). Further much of the sinking
530 POC flux was in the form of small particles driven by mesozooplankton processesing (Durkin et
531 al., 2021; Amaral et al. 2022; McNair et al., 2023; Shea et al. 2023), as marine snow aggregates
532 (> 0.5 mm) were not found in any of the Marine Snow Catcher deployments (Romanelli et al.,
533 2024). Durkin et al., (2021) used sediment traps equipped with polyacrylamide gel layers found
534 that small particles (< 100 μm) contributed on average 17% ($\pm 9\%$ s.d.) of total POC flux in the

535 upper 500 m. However, Estapa et al., (2021) concluded that traps undercollected small particles
536 due to hydrodynamic effects (Buesseler et al., 2007), suggesting that the contribution of particles
537 too small to be sampled by the UVP may have been higher. This may be an issue as flux values
538 calculated from UVPs are highly sensitive to small particle abundances (Bisson et al., 2022).
539 Recent work by Clements et al., (2023) has demonstrated that extending the UVP's size range to
540 smaller sizes using power-law extrapolation reduced bias in flux estimates and this procedure
541 should be considered in future work.

542 Large marine snow-sized (≥ 5 mm) aggregates were rarely, if ever, sampled by the UVPs during
543 the NP deployment (Figures 1 and S1). However, it was observed that the rare occurrence of salps
544 and their very large fecal pellets (≥ 4 mm; see Figure 2d in Steinberg et al., (2023)) had an
545 inordinately large contribution to sinking POC fluxes (Durkin et al., 2021; Steinberg et al., 2023).
546 Notably, during E1, salp fecal pellet export contributed 48 to nearly 90% of the modeled total
547 POC flux (Steinberg et al., 2023), which happens to coincide with the largest discrepancies
548 between UVP-based and ^{234}Th -derived POC fluxes and, to a lower extent, traps (Figure 3f). The
549 UVPs rarely observed large salp pellets due to the ephemeral occurrence of salp populations,
550 their rapid sinking speeds and the relatively small sampling volume of the UVP (Steinberg et al.,
551 2023). Thus, significant underestimation of POC flux due to the potential under sampling of salp
552 fecal pellets by UVP imaging likely would lead to misleading conclusions about carbon export
553 dynamics. Estapa et al., (2021) also concluded that traps under collected rare larger particles,
554 including salp fecal pellets, which would make the trap POC flux results too low. The ephemeral
555 nature of salp populations and their impacts on sinking POC fluxes may also explain the
556 fluctuating nature of UVP-derived POC flux profiles versus depth and their large cast-to-cast
557 variations (Figure 3).

558 It should also mentioned that the detection of rare living organisms by the UVP will introduce
559 uncertainty into flux calculations (Bisson et al., 2022). For example, Kiko et al., (2020) found that
560 excluding living organisms and artifacts larger than 1 mm from the UVP5 dataset decreased the
561 variability of PSD-derived POC flux estimates. Here, morphological classifications of UVP images
562 were made on a subset of the EXPORTS NP UVP data found a fairly low contribution from living
563 organisms (~9%) from the total number of particles larger than 1 mm imaged (A. McDonnell,
564 pers. comm., 2020). Although it is small, the fraction of large particles that were living in the NP
565 is considerably larger than what was found in the NA (< 1%; Drago, 2023). Again, the observations
566 of these very large particles in UVP5 PSD will be rare, thereby minimally influencing the
567 uncertainties in UVP flux determinations (Bisson et al., 2022; Kiko et al., 2020).

568 4.3.2 Insights from the NA

569 As the NA deployment was highly dynamic taking place during the demise of the North Atlantic
570 spring bloom (Johnson et al., 2024; Romanelli et al., 2024; Siegel et al., 2025), discrepancies in
571 the UVP-based POC fluxes are likely due to temporal factors (SI, Figure S4). Briefly, during E1 (May
572 5-7, storm 1 on May 7-11), export fluxes were low across most measures, including sediment
573 traps and ^{234}Th (Figure 4), and no aggregates were found in the Marine Snow Catcher (Romanelli
574 et al., 2024). After storm 2 (May 15) in E2 (May 11-20), aggregates were collected in the Marine
575 Snow Catchers, but export fluxes increased some, until E3 (May 21-29), when large particles

576 substantially increased, particularly at depth (Fig 4; see also Figure 2a in (Romanelli et al., 2024).
577 Shifts in the dominant plankton community, from large diatoms to a more diverse phytoplankton
578 community were also observed (Meyer et al. 2024; San Soucie et al. 2024). Throughout the NA
579 experiment, particles were consistently fluffy and porous, becoming progressively fluffier and
580 more porous as the cruise progressed (Siegel et al., 2025). Analysis of the morphology of
581 individual large (≥ 1 mm) particles sampled in the images collected by the UVP showed that fluffy
582 aggregates dominated the dataset, accounting for 88% of the particles analyzed, while dense
583 aggregates (10%), fecal pellets (1%), zooplankton pellets (1%) and living organisms (0.7%) made
584 up the rest (Drago, 2023).

585 Given the evolving conditions, the average of the UVP profiles effectively captured the bloom
586 stages, mirroring the trap results, both of which increase in E3 (Figures 4a-d). POC fluxes from
587 the traps varied by an order of magnitude between E1 and E3, which allowed us to effectively
588 train UVPs to translate observed PSD changes into POC fluxes. However, the performance of the
589 ^{234}Th -derived POC fluxes was poor for both the global and regional tuning (Figures 4e-h).
590 Differences in between traps and ^{234}Th in the NA have previously been reported at the EXPORTS
591 sampling site and were linked to the persistence of ^{234}Th disequilibrium in the water column prior
592 to sampling (Ceballos-Romero et al., 2016, 2018). Clevenger et al. (2024) suggest that the ^{234}Th
593 profiles sampled during the EXPORTS cruise reflect both an earlier export event in addition to the
594 evolving conditions during the cruise (see also Johnson et al., (2024)). We conclude that the prior
595 export likely contributed to the differences observed in the UVP flux calibration between traps
596 and ^{234}Th in the NA. We see this both in shallow and deeper depths. The ^{234}Th deficit at depth
597 indicates that export had reached deeper waters from the previous time-period. This explains
598 the much higher ^{234}Th -derived POC fluxes compared to traps and UVPs at depth. The export from
599 the first bloom also would influence the calibration of A and B coefficients using ^{234}Th , at the
600 same time leading to the low predictive power for the regional NA ^{234}Th method. Fluxes based
601 upon ^{234}Th do increase in E3 but are not reflected in the UVP particle fields that are responding
602 more quickly. Therefore, in highly dynamic and non-steady state environments like the NA,
603 changing ^{234}Th distributions to the evolving particle fields measured by UVPs.

604 5 Next steps

605 The present results suggest improvements in estimating sinking POC fluxes from in situ imagery
606 requires incorporating more information about the particle field than just size distribution. Eq.
607 (1) shows that POC fluxes could be calculated directly from the size distribution, $N(D)$, only if the
608 size dependence of particle carbon content, $\rho_{POC}(D)$ and its sinking rate, $w_s(D)$, are well
609 constrained. Therefore, it seems important to better characterize these properties.

610 Moving forward, we propose exploring alternative approaches that consider particle
611 morphologies - such as transparency, shape, and structure -, and geochemical characteristics -
612 such as elemental composition, pigments content, and the nature of organic matter - for more
613 accurate UVP-based POC flux estimates. Next-generation UVPs could also integrate optical
614 measurements, such as particle fluorescence, to provide proxies for some of these properties.
615 Relying on particle size alone neglects the influence of traits that influence sinking behavior and
616 carbon content and thus contributes to export variations over time and depth. For example, the

617 optical properties of particles, particularly their index of refraction, are linked to their carbon
618 content, as demonstrated in phytoplankton (Stramski, 1999), and this likely hold true for other
619 types of particles such as zooplankton and detritus, where darker particles have been associated
620 with higher carbon content (Durkin et al., 2021). Recent studies also show that transparency and
621 body size can influence particle behavior in the water column, including vertical migration and
622 carbon transport to depth (Barth et al., 2023), while mesozooplankton morphological and
623 taxonomic diversity plays a key role in regional variability of carbon export (Perhirin et al., 2024).
624 Furthermore, Laurenceau-Cornec et al., (2015) demonstrated that sinking velocities correlate not
625 just with size but also with morphology and aggregate structure, with site-dependent ecological
626 factors and dominant phytoplankton morphologies strongly influencing particle sinking rates and
627 carbon export efficiency. More recent findings emphasize that mineral ballasting and porosity
628 critically modulate aggregate sinking velocities, challenging classical Stokes' Law assumptions,
629 especially in the mesopelagic zone where organic-to-mineral ratios vary (Laurenceau-Cornec et
630 al., 2020). Together, these insights highlight the need to consider biological, ecological, and
631 compositional traits beyond size to enhance our understanding and modeling of particle
632 composition and its role in carbon export.

633 It is also important to recognize that unsorted PSD data reflect standing stocks, which may or
634 may not accurately reflect real POC fluxes. At a minimum, particles should be categorized as living
635 and non-living, ideally with a more detailed classification considering different particle types
636 across the water column. Large variability between individual UVP profiles is common, suggesting
637 that only the mean of multiple profiles can reliably estimate local fluxes. Moreover, because UVP
638 profiles represent particle stocks rather than net fluxes, absolute UVP-based POC flux values near
639 the shallowest depths (Figures 3 and 4) can appear unrealistically high and continue to increase
640 toward the surface. Shallower values should therefore be interpreted with caution. To minimize
641 this issue, fluxes above the mixed layer were arbitrarily excluded. Finally, we recommend further
642 studies to compare UVP-based POC flux with estimates from gel traps and include morphological
643 sorting of sinking particles, as introduced in Trudnowska et al., (2021). Such a combined approach
644 could enhance the accuracy of UVP-based POC flux estimates by better distinguishing particle
645 types and identifying dominant morphological groups specific to each site and time.

646 It is hoped that the next generation of in situ particle imaging systems will incorporate these
647 morphological, optical, and geochemical features, enabling more precise and mechanistically
648 informed estimates of particle fluxes and their variability in the ocean, ultimately advancing our
649 understanding of carbon export dynamics in marine environments.

650 Finally, depth-constant A and B coefficients were applied throughout the water column for
651 consistency across sites. However, variations in particle composition and sinking speed with
652 depth (e.g., Amaral et al., 2022, 2024) could lead to depth-dependent relationships between
653 particle size and POC content. We therefore recommend that future studies explore depth-
654 resolved A and B coefficients to better capture vertical variability in particle characteristics.

655 **6 Conclusions**

656 We systematically calibrated large UVP-based PSD data against co-located sediment trap and
657 ^{234}Th flux observations and applied this approach across biogeochemically distinct sites in the NA

658 and NP at both global and regional scales. Our results show that UVP-based POC flux estimates
659 effectively capture broad-scale spatial (NP vs. NA) and temporal (early versus late bloom stages)
660 variations but struggle to resolve finer vertical, temporal, and regional changes. We conclude
661 that in the NP, the limited predictive power reflects small changes in the magnitude of the POC
662 flux observations used to calibrate UVP data and the disproportionate contribution of rare large
663 particles to the flux, while in the NA, sediment trap calibrations outperformed ^{234}Th -based ones
664 due to complexities in ^{234}Th deficits and mismatches between UVP particle stocks and fluxes
665 under non-steady-state conditions. We highlight the need for further calibration studies with
666 ^{234}Th to better assess its utility in variable conditions and suggest exploring UVP use for tracking
667 changes in particle stocks over time rather than assuming that higher stocks reflect higher fluxes.

668 Despite the value of current calibrations, challenges remain due to imaging size and resolution
669 limits, methodological uncertainties, and variability in the calibration coefficients (A and B) -
670 which can differ by location, depth, time, and particle size range - sometimes resulting in flux
671 estimate errors exceeding 50%, with variations in A and B across studies sometimes causing
672 order-of-magnitude differences in predicted POC flux (Figure 5). We caution against deriving A
673 and B from a few UVP profiles due to data variability and recommend fitting these coefficients
674 using extensive co-located observations. Where data are limited, for consistency in broader-scale
675 applications using in situ imagery from a size range similar to that discussed in this study (128 μm
676 - 26 mm) and at depths between the mixed layer and 500 m, we suggest users consider the
677 coefficients derived here, specifically the "global approach using traps" for global applications,
678 and the "regional approach using traps NA" for studies focused on the NA region (Table 1).
679 However, we stress that these recommendations are not meant to exclude other approaches.
680 Rather, they reflect the best available fits from our dataset. We encourage further work
681 incorporating more co-located observations across regions and conditions to refine A and B
682 coefficients for more robust and reliable assessments of sinking particle export fluxes from PSD
683 data.

684 **Acknowledgments**

685 This work was supported by NASA Ocean Biology and Biogeochemistry program, the National
686 Science Foundation Biological and Chemical Oceanography programs and the Woods Hole
687 Oceanographic Institution's Ocean Twilight Zone study. We greatly acknowledge the
688 cooperation, skill and commitment of the Captains, Crews, Research Technicians and
689 Administrative Staffs of the R/V Roger Revelle (RR1813), R/V Sally Ride (SR1812), RRS James Cook
690 (JC214), RRS Discovery (DY131) and the R/V Sarmiento de Gamboa (SdG2105). This project has
691 received funding from the European Union's Horizon 2020 research and innovation programme
692 under the Marie Skłodowska-Curie grant agreement No 101032903. RK acknowledges support
693 via a "Make Our Planet Great Again" grant of the French National Research Agency within the
694 "Program d'Investissements d'Avenir"; reference "ANR-19MPGA-0012" and funding from the
695 Heisenberg Programme of the German Science Foundation #KI 1387/5-1.

696 **Data Availability Statement**

697 NASA-funded primary data products are archived at SeaWiFS Bio-optical Archive and Storage
698 System (SeaBASS). All EXPORTS data are being archived under one digital object identifier (DOI:
699 <http://dx.doi.org/10.5067/SeaBASS/EXPORTS/DATA001>) that further expands into the individual

700 data subsets. NSF-funded. To find out information about all the data collected during the
701 EXPORTS field campaigns, their data repositories and availability, please visit:
702 <https://sites.google.com/view/oceanexports/home>. All data used in this study, along with
703 MATLAB files for data analysis and visualization, are available under the DOI:
704 <https://doi.org/10.6084/m9.figshare.28410668.v3> by Fields & Siegel, 2025.

705 **References**

706 Alldredge, A. (1998). The carbon, nitrogen and mass content of marine snow as a function of
707 aggregate size. *Deep Sea Research Part I: Oceanographic Research Papers*, 45(4–5), 529–
708 541. [https://doi.org/10.1016/S0967-0637\(97\)00048-4](https://doi.org/10.1016/S0967-0637(97)00048-4)

709 Alldredge, A. L., & Gotschalk, C. (1988). In situ settling behavior of marine snow. *Limnology and*
710 *Oceanography*, 33(3), 339–351. <https://doi.org/10.4319/lo.1988.33.3.0339>

711 Amaral, V. J., Lam, P. J., Marchal, O., Roca-Martí, M., Fox, J., & Nelson, N. B. (2022). Particle
712 cycling rates at Station P as estimated from the inversion of POC concentration data.
713 *Elementa: Science of the Anthropocene*, 10(1), 1415–1428.
714 <https://doi.org/10.1525/elementa.2021.00018>

715 Amaral, V. J., Lam, P. J., Marchal, O., & Kenyon, J. A. (2024). Cycling Rates of Particulate Organic
716 Carbon Along the GEOTRACES Pacific Meridional Transect GP15. *Global Biogeochemical*
717 *Cycles*, 38(1), e2023GB007940. <https://doi.org/10.1029/2023GB007940>

718 Barth, A., Johnson, R., & Stone, J. (2023). Size and transparency influence diel vertical migration
719 patterns in copepods. *Limnology and Oceanography*, 68(12), 2749–2758.
720 <https://doi.org/10.1002/lo.12461>

721 Bisson, K. M., Siegel, D. A., DeVries, T., Cael, B. B., & Buesseler, K. O. (2018). How Data Set
722 Characteristics Influence Ocean Carbon Export Models. *Global Biogeochemical Cycles*,
723 32(9), 1312–1328. <https://doi.org/10.1029/2018GB005934>

724 Bisson, Kelsey M., Kiko, R., Siegel, D. A., Guidi, L., Picheral, M., Boss, E., & Cael, B. B. (2022).
725 Sampling uncertainties of particle size distributions and derived fluxes. *Limnology and*
726 *Oceanography: Methods*, 2022. <https://doi.org/10.1002/lom3.10524>

727 Boyd, P. W., & Trull, T. W. (2007). Understanding the export of biogenic particles in oceanic
728 waters: Is there consensus? *Progress in Oceanography*, 72(4), 276–312.
729 <https://doi.org/10.1016/j.pocean.2006.10.007>

730 Boyd, Philip W., Claustre, H., Levy, M., Siegel, D. A., & Weber, T. (2019). Multi-faceted particle
731 pumps drive carbon sequestration in the ocean. *Nature*, 568(7752), 327–335.
732 <https://doi.org/10.1038/s41586-019-1098-2>

733 Brzezinski, M. A., Johnson, L., Estapa, M., Clevenger, S., Roca-Martí, M., Romanelli, E., et al.
734 (2024). Physical Mechanisms Sustaining Silica Production Following the Demise of the
735 Diatom Phase of the North Atlantic Spring Phytoplankton Bloom During EXPORTS. *Global*
736 *Biogeochemical Cycles*, 38(7), e2023GB008048. <https://doi.org/10.1029/2023GB008048>

737 Buesseler, K. O., Benitez-Nelson, C. R., Moran, S. B., Burd, A., Charette, M., Cochran, J. K., et al.
738 (2006). An assessment of particulate organic carbon to thorium-234 ratios in the ocean
739 and their impact on the application of ^{234}Th as a POC flux proxy. *Marine Chemistry*, 100(3-
740 4 SPEC. ISS.), 213–233. <https://doi.org/10.1016/j.marchem.2005.10.013>

741 Buesseler, Ken O., Bacon, M. P., Kirk Cochran, J., & Livingston, H. D. (1992). Carbon and nitrogen
742 export during the JGOFS North Atlantic Bloom experiment estimated from ^{234}Th : ^{238}U
743 disequilibria. *Deep Sea Research Part A, Oceanographic Research Papers*, 39(7–8), 1115–
744 1137. [https://doi.org/10.1016/0198-0149\(92\)90060-7](https://doi.org/10.1016/0198-0149(92)90060-7)

745 Buesseler, Ken O., Antia, A. N., Chen, M., Fowler, S. W., Gardner, W. D., Gustafsson, O., et al.
746 (2007). An assessment of the use of sediment traps for estimating upper ocean particle
747 fluxes. *Journal of Marine Research*, 65(3), 345–416.
748 <https://doi.org/10.1357/002224007781567621>

749 Buesseler, Ken O., Benitez-Nelson, C. R., Roca-Martí, M., Wyatt, A. M., Resplandy, L., Clevenger,
750 S. J., et al. (2020). High-resolution spatial and temporal measurements of particulate
751 organic carbon flux using thorium-234 in the northeast Pacific Ocean during the EXport
752 Processes in the Ocean from RemoTe Sensing field campaign. *Elementa: Science of the
753 Anthropocene*, 8(1). <https://doi.org/10.1525/elementa.030>

754 Buesseler, Ken O., Boyd, P. W., Black, E. E., & Siegel, D. A. (2020). Metrics that matter for
755 assessing the ocean biological carbon pump. *Proceedings of the National Academy of
756 Sciences of the United States of America*, 117(18), 9679–9687.
757 <https://doi.org/10.1073/pnas.1918114117>

758 Ceballos-Romero, E., Le Moigne, F. A. C., Henson, S., Marsay, C. M., Sanders, R. J., García-
759 Tenorio, R., & Villa-Alfageme, M. (2016). Influence of bloom dynamics on Particle Export
760 Efficiency in the North Atlantic: a comparative study of radioanalytical techniques and
761 sediment traps. *Marine Chemistry*, 186, 198–210.
762 <https://doi.org/10.1016/j.marchem.2016.10.001>

763 Ceballos-Romero, E., De Soto, F., Le Moigne, F. A. C., García-Tenorio, R., & Villa-Alfageme, M.
764 (2018). ^{234}Th -Derived Particle Fluxes and Seasonal Variability: When Is the SS Assumption
765 Reliable? Insights From a Novel Approach for Carbon Flux Simulation. *Geophysical
766 Research Letters*, 45(24), 13,414–13,426. <https://doi.org/10.1029/2018GL079968>

767 Clements, D. J., Yang, S., Weber, T., McDonnell, A. M. P., Kiko, R., Stemmann, L., & Bianchi, D.
768 (2022). Constraining the Particle Size Distribution of Large Marine Particles in the Global
769 Ocean With In Situ Optical Observations and Supervised Learning. *Global Biogeochemical
770 Cycles*, 36(5), e2021GB007276. <https://doi.org/10.1029/2021GB007276>

771 Clements, D. J., Yang, S., Weber, T., McDonnell, A. M. P., Kiko, R., Stemmann, L., & Bianchi, D.
772 (2023). New Estimate of Organic Carbon Export From Optical Measurements Reveals the
773 Role of Particle Size Distribution and Export Horizon. *Global Biogeochemical Cycles*, 37(3),
774 1–21. <https://doi.org/10.1029/2022GB007633>

775 Clevenger, S. J., Benitez-Nelson, C. R., Drysdale, J., Pike, S., Puigcorbé, V., & Buesseler, K. O.

776 (2021). Review of the analysis of ^{234}Th in small volume (2–4 L) seawater samples:
777 improvements and recommendations. *Journal of Radioanalytical and Nuclear Chemistry*,
778 329(1). <https://doi.org/10.1007/s10967-021-07772-2>

779 Clevenger, S. J., Benitez-Nelson, C. R., Roca-Martí, M., Bam, W., Estapa, M., Kenyon, J. A., et al.
780 (2024). Carbon and silica fluxes during a declining North Atlantic spring bloom as part of
781 the EXPORTS program. *Marine Chemistry*, 258, 104346.
782 <https://doi.org/10.1016/j.marchem.2023.104346>

783 Cram, J. A., Fuchsman, C. A., Duffy, M. E., Pretty, J. L., Lekanoff, R. M., Neibauer, J. A., et al.
784 (2022). Slow Particle Remineralization, Rather Than Suppressed Disaggregation, Drives
785 Efficient Flux Transfer Through the Eastern Tropical North Pacific Oxygen Deficient Zone.
786 *Global Biogeochemical Cycles*, 36(1). <https://doi.org/10.1029/2021GB007080>

787 Drago, L. (2023). *Analyse globale de la pompe à carbone biologique à partir de données en*
788 *imagerie quantitative*. Retrieved from <http://www.theses.fr/2023SORUS562/document>

789 Durkin, C. A., Buesseler, K. O., Cetinić, I., Estapa, M. L., Kelly, R. P., & Omand, M. (2021). A Visual
790 Tour of Carbon Export by Sinking Particles. *Global Biogeochemical Cycles*, 35(10),
791 2021.02.16.431317. <https://doi.org/10.1029/2021GB006985>

792 Eppley, R. W., & Peterson, B. J. (1979). Particulate organic matter flux and planktonic new
793 production in the deep ocean. *Nature*, 282(5740), 677–680.
794 <https://doi.org/10.1038/282677a0>

795 Erickson, Z. K., Fields, E., Johnson, L., Thompson, A. F., Lilian, A., Asaro, E. A. D., & Siegel, D. A.
796 (2023). Eddy tracking from in situ and satellite observations. *ESS Open Archive*.
797 <https://doi.org/10.22541/essoar.167979672.22588418/v1>

798 Estapa, M., Buesseler, K., Durkin, C. A., Omand, M., Benitez-Nelson, C. R., Roca-Martí, M., et al.
799 (2021). Biogenic sinking particle fluxes and sediment trap collection efficiency at Ocean
800 Station Papa. *Elementa*, 9(1). <https://doi.org/10.1525/elementa.2020.00122>

801 Fender, C. K., Kelly, T. B., Guidi, L., Ohman, M. D., Smith, M. C., & Stukel, M. R. (2019).
802 Investigating Particle Size-Flux Relationships and the Biological Pump Across a Range of
803 Plankton Ecosystem States From Coastal to Oligotrophic. *Frontiers in Marine Science*, 6,
804 603. <https://doi.org/10.3389/fmars.2019.00603>

805 Fields, E., & Siegel, D. A. (2025). data and code used for On the assessment of sinking particle
806 fluxes from in situ aggregate size distribution observations by Elena Ceballos Romero and
807 others - preprint at <https://doi.org/10.31223/X5899D>.
808 <https://doi.org/10.6084/m9.figshare.28410668.v1>

809 Forest, A., Babin, M., Stemmann, L., Picheral, M., Sampei, M., Fortier, L., et al. (2013).
810 Ecosystem function and particle flux dynamics across the Mackenzie Shelf (Beaufort Sea,
811 Arctic Ocean): an integrative analysis of spatial variability and biophysical forcings.
812 *Biogeosciences*, 10(5), 2833–2866. <https://doi.org/10.5194/bg-10-2833-2013>

813 Giering, S. L. C., Hosking, B., Briggs, N., & Iversen, M. H. (2020). The Interpretation of Particle

814 Size, Shape, and Carbon Flux of Marine Particle Images Is Strongly Affected by the Choice
815 of Particle Detection Algorithm. *Frontiers in Marine Science*, 7, 564.
816 <https://doi.org/10.3389/fmars.2020.00564>

817 Guidi, L., Jackson, G. A., Stemmann, L., Miquel, J. C., Picheral, M., & Gorsky, G. (2008).
818 Relationship between particle size distribution and flux in the mesopelagic zone. *Deep-Sea*
819 *Research Part I: Oceanographic Research Papers*, 55(10), 1364–1374.
820 <https://doi.org/10.1016/j.dsr.2008.05.014>

821 Guidi, L., Stemmann, L., Jackson, G. A., Ibanez, F., Claustre, H., Legendre, L., et al. (2009). Effects
822 of phytoplankton community on production, size, and export of large aggregates: A world-
823 ocean analysis. *Limnology and Oceanography*, 54(6), 1951–1963.
824 <https://doi.org/10.4319/lo.2009.54.6.1951>

825 Guidi, L., Legendre, L., Reygondeau, G., Uitz, J., Stemmann, L., & Henson, S. A. (2015). A new
826 look at ocean carbon remineralization for estimating deepwater sequestration. *Global*
827 *Biogeochemical Cycles*, 29(7), 1044–1059. <https://doi.org/10.1002/2014GB005063>

828 Guidi, L., Chaffron, S., Bittner, L., Eveillard, D., Larhlimi, A., Roux, S., et al. (2016). Plankton
829 networks driving carbon export in the oligotrophic ocean. *Nature*, 532(7600), 465–470.
830 <https://doi.org/10.1038/nature16942>

831 Iversen, M. H., Nowald, N., Ploug, H., Jackson, G. A., & Fischer, G. (2010). High resolution
832 profiles of vertical particulate organic matter export off Cape Blanc, Mauritania:
833 Degradation processes and ballasting effects. *Deep-Sea Research Part I: Oceanographic*
834 *Research Papers*, 57(6), 771–784. <https://doi.org/10.1016/j.dsr.2010.03.007>

835 Johnson, L., Siegel, D. A., Thompson, A. F., Fields, E., Erickson, Z. K., Cetinic, I., et al. (2024).
836 Assessment of oceanographic conditions during the North Atlantic EXport processes in the
837 ocean from RemoTe sensing (EXPORTS) field campaign. *Progress in Oceanography*, 220,
838 103170. <https://doi.org/10.1016/j.pocean.2023.103170>

839 Kiko, R., Biastoch, A., Brandt, P., Cravatte, S., Hauss, H., Hummels, R., et al. (2017). Biological
840 and physical influences on marine snowfall at the equator. *Nature Geoscience*, 10(11),
841 852–858. <https://doi.org/10.1038/NGEO3042>

842 Kiko, Rainer, Brandt, P., Christiansen, S., Faustmann, J., Kriest, I., Rodrigues, E., et al. (2020).
843 Zooplankton-Mediated Fluxes in the Eastern Tropical North Atlantic. *Frontiers in Marine*
844 *Science*, 7(May), 1–21. <https://doi.org/10.3389/fmars.2020.00358>

845 Kiko, Rainer, Picheral, M., Antoine, D., Babin, M., Berline, L., Biard, T., et al. (2022). A global
846 marine particle size distribution dataset obtained with the Underwater Vision Profiler 5
847 (Discussion). *Earth System Science Data Discussions*, 14(9), 4315–4337.
848 <https://doi.org/10.5194/essd-2022-51>

849 Kriest, I. (2002). Different parameterizations of marine snow in a 1D-model and their influence
850 on representation of marine snow, nitrogen budget and sedimentation. *Deep Sea Research*
851 *Part I: Oceanographic Research Papers*, 49(12), 2133–2162.

852 [https://doi.org/10.1016/S0967-0637\(02\)00127-9](https://doi.org/10.1016/S0967-0637(02)00127-9)

853 De La Rocha, C. L., & Passow, U. (2007). Factors influencing the sinking of POC and the efficiency
854 of the biological carbon pump. *Deep-Sea Research Part II: Topical Studies in Oceanography*,
855 54(5–7), 639–658. <https://doi.org/10.1016/j.dsr2.2007.01.004>

856 Laurenceau-Cornec, E., Trull, T., Davies, D., De La Rocha, C., & Blain, S. (2015). Phytoplankton
857 morphology controls on marine snow sinking velocity. *Marine Ecology Progress Series*, 520,
858 35–56. <https://doi.org/10.3354/meps11116>

859 Laurenceau-Cornec, E. C., Le Moigne, F. A. C., Gallinari, M., Moriceau, B., Toullec, J., Iversen, M.
860 H., et al. (2020). New guidelines for the application of Stokes' models to the sinking
861 velocity of marine aggregates. *Limnology and Oceanography*, 65(6), 1264–1285.
862 <https://doi.org/10.1002/1no.11388>

863 Logan, B. E., & Kilps, J. R. (1995). Fractal dimensions of aggregates formed in different fluid
864 mechanical environments. *Water Research*, 29(2), 443–453. [https://doi.org/10.1016/0043-1354\(94\)00186-B](https://doi.org/10.1016/0043-1354(94)00186-B)

866 Logan, B. E., & Wilkinson, D. B. (1990). Fractal geometry of marine snow and other biological
867 aggregates. *Limnology and Oceanography*, 35(1), 130–136.
868 <https://doi.org/10.4319/lo.1990.35.1.0130>

869 Lombard, F., & Kiørboe, T. (2010). Marine snow originating from appendicularian houses: Age-
870 dependent settling characteristics. *Deep Sea Research Part I: Oceanographic Research
871 Papers*, 57(10), 1304–1313. <https://doi.org/10.1016/j.dsr.2010.06.008>

872 McDonnell, A. M. P., & Buesseler, K. O. (2010). Variability in the average sinking velocity of
873 marine particles. *Limnology and Oceanography*, 55(5), 2085–2096.
874 <https://doi.org/10.4319/lo.2010.55.5.2085>

875 McNair, H. M., Meyer, M. G., Lerch, S. J., Maas, A. E., Stephens, B. M., Fox, J., et al. (2023).
876 Quantitative analysis of food web dynamics in a low export ecosystem. *BioRxiv*,
877 2023.03.17.532807. <https://doi.org/10.1101/2023.03.17.532807>

878 Perhirin, M., Gossner, H., Godfrey, J., Johnson, R., Blanco-Bercial, L., & Ayata, S. (2024).
879 Morphological and taxonomic diversity of mesozooplankton is an important driver of
880 carbon export fluxes in the ocean. *Molecular Ecology Resources*, 24(2), e13907.
881 <https://doi.org/10.1111/1755-0998.13907>

882 Picheral, M., Guidi, L., Stemmann, L., Karl, D. M., Iddaoud, G., & Gorsky, G. (2010). The
883 underwater vision profiler 5: An advanced instrument for high spatial resolution studies of
884 particle size spectra and zooplankton. *Limnology and Oceanography: Methods*, 8(SEPT),
885 462–473. <https://doi.org/10.4319/lom.2010.8.462>

886 Picheral, M., Catalano, C., Brousseau, D., Claustre, H., Coppola, L., Leymarie, E., et al. (2022).
887 <scp>The Underwater Vision Profiler 6: an imaging sensor of particle size spectra and
888 plankton, for autonomous and cabled platforms</scp>. *Limnology and Oceanography:
889 Methods*, 20(2), 115–129. <https://doi.org/10.1002/lom3.10475>

890 Ramondenc, S., Madeleine, G., Lombard, F., Santinelli, C., Stemmann, L., Gorsky, G., & Guidi, L.
891 (2016). An initial carbon export assessment in the Mediterranean Sea based on drifting
892 sediment traps and the Underwater Vision Profiler data sets. *Deep-Sea Research Part I: Oceanographic Research Papers*, 117, 107–119. <https://doi.org/10.1016/j.dsr.2016.08.015>

893

894 Romanelli, E., Giering, S. L. C., Estapa, M., Siegel, D. A., & Passow, U. (2024). Can intense storms
895 affect sinking particle dynamics after the North Atlantic spring bloom? *Limnology and
896 Oceanography*, 2024.01.11.575202. <https://doi.org/10.1002/lo.12723>

897 Savoye, N., Benitez-Nelson, C., Burd, A. B., Cochran, J. K., Charette, M., Buesseler, K. O., et al.
898 (2006). ²³⁴Th sorption and export models in the water column: A review. *Marine Chemistry*, 100(3-4 SPEC. ISS.), 234–249. <https://doi.org/10.1016/j.marchem.2005.10.014>

899

900 Seber, G. A. F., & Wild, C. J. (2003). *Nonlinear Regression*. Wiley. New York: Wiley. Retrieved
901 from <http://as.wiley.com/WileyCDA/WileyTitle/productCd-0471471356.html>

902 Sheldon, R. W., Prakash, A., & Sutcliffe, H. (1972). The size distribution of particles in the ocean.
903 *Limnology and Oceanography*, XVII(MAY), 327–340.

904 Siegel, D., Burd, A., Estapa, M., Fields, E., Johnson, L., Romanelli, E., et al. (2024). Dynamics of
905 Aggregates and Sinking Carbon Fluxes in a Turbulent Ocean. *EarthArXiv Eprints*.
906 <https://doi.org/10.31223/X58709>

907 Siegel, D., Burd, A., Estapa, M., Fields, E., Johnson, L., Romanelli, E., et al. (2025, May 21).
908 Assessing Marine Snow Dynamics During the Demise of the North Atlantic Spring Bloom
909 Using In Situ Particle Imagery. *EarthArXiv*. <https://doi.org/10.31223/X58709>

910 Siegel, D. A., Fields, E., & Buesseler, K. O. (2008). A bottom-up view of the biological pump:
911 Modeling source funnels above ocean sediment traps. *Deep-Sea Research Part I: Oceanographic Research Papers*, 55(1), 108–127.
912 <https://doi.org/10.1016/j.dsr.2007.10.006>

913

914 Siegel, David A., Buesseler, K. O., Behrenfeld, M. J., Benitez-Nelson, C. R., Boss, E., Brzezinski, M.
915 A., et al. (2016). Prediction of the export and fate of global ocean net primary production:
916 The exports science plan. *Frontiers in Marine Science*, 3(MAR).
917 <https://doi.org/10.3389/fmars.2016.00022>

918 Siegel, David A., Cetinić, I., Graff, J. R., Lee, C. M., Nelson, N., Perry, M. J., et al. (2021). An
919 operational overview of the EXport Processes in the Ocean from RemoTe Sensing
920 (EXPORTS) Northeast Pacific field deployment. *Elementa: Science of the Anthropocene*,
921 9(1). <https://doi.org/10.1525/elementa.2020.00107>

922 Siegel, David A., Cetinic, I., Thompson, A. F., Nelson, N. B., Sten, M., Omand, M., et al. (2023).
923 *EXport Processes in the Ocean from RemoTe Sensing (EXPORTS) North Atlantic sensor
924 calibration and intercalibration documents*. <https://doi.org/10.1575/1912/66998>

925 Siegel, David A., DeVries, T., Cetinić, I., & Bisson, K. M. (2023). Quantifying the Ocean's
926 Biological Pump and Its Carbon Cycle Impacts on Global Scales. *Annual Review of Marine
927 Science*, 15(1), 329–356. <https://doi.org/10.1146/annurev-marine-040722-115226>

928 Soucie, J. E. S., Sosik, H. M., Girdhar, Y., Shalapyonok, A., Peacock, E., & Johnson, L.
929 Spatiotemporal Topic Modeling Reveals Storm-Driven Advection and Stirring Control
930 Plankton Community Variability in an Open Ocean Eddy. *Authorea Preprints*.
931 <https://doi.org/10.22541/ESSOAR.171415914.42561749/V1>

932 Stamieszkin, K., Steinberg, D. K., & Maas, A. E. (2021). Fecal pellet production by
933 mesozooplankton in the subarctic Northeast Pacific Ocean. *Limnology and Oceanography*,
934 66(7), 2585–2597. <https://doi.org/10.1002/lno.11774>

935 Steinberg, D. K., Stamieszkin, K., Maas, A. E., Durkin, C. A., Passow, U., Estapa, M. L., et al.
936 (2023). The Outsized Role of Salps in Carbon Export in the Subarctic Northeast Pacific
937 Ocean. *Global Biogeochemical Cycles*, 37(1), e2022GB007523.
938 <https://doi.org/10.1029/2022GB007523>

939 Stemmann, L., & Boss, E. (2012). Plankton and particle size and packaging: From determining
940 optical properties to driving the biological pump. *Annual Review of Marine Science*, 4(1),
941 263–290. <https://doi.org/10.1146/annurev-marine-120710-100853>

942 Stramski, D. (1999). Refractive index of planktonic cells as a measure of cellular carbon and
943 chlorophyll a content. *Deep Sea Research Part I: Oceanographic Research Papers*, 46(2),
944 335–351. [https://doi.org/10.1016/S0967-0637\(98\)00065-X](https://doi.org/10.1016/S0967-0637(98)00065-X)

945 Trudnowska, E., Lacour, L., Ardyna, M., Rogge, A., Irisson, J. O., Waite, A. M., et al. (2021).
946 Marine snow morphology illuminates the evolution of phytoplankton blooms and
947 determines their subsequent vertical export. *Nature Communications*, 12(1), 2816.
948 <https://doi.org/10.1038/s41467-021-22994-4>

949 Turner, J. T. (2015). Zooplankton fecal pellets, marine snow, phytodetritus and the ocean's
950 biological pump. *Progress in Oceanography*, 130(1), 205–248.
951 <https://doi.org/10.1016/j.pocean.2014.08.005>

952